Available online at www.sciencedirect.com
SCIENCE DIRECT®
Journal of Computational Physics 205 (2005) 205–221
JOURNAL OF COMPUTATIONAL PHYSICS
www.elsevier.com/locate/jcp

A robust, colocated, implicit algorithm for direct numerical simulation of compressible, turbulent flows

Yucheng Hou, Krishnan Mahesh *

Department of Aerospace Engineering and Mechanics, 107 Akerman Hall, 110 Union Street SE, Minneapolis MN 55455, USA

Received 18 January 2004; received in revised form 24 August 2004; accepted 27 October 2004
Available online 10 December 2004

Abstract

A non-dissipative, robust, implicit algorithm is proposed for direct numerical and large-eddy simulation of compressible turbulent flows. The algorithm addresses the problems caused by low Mach numbers and under-resolved high Reynolds numbers. It colocates variables in space to allow easy extension to unstructured grids, and discretely conserves mass, momentum and total energy. The Navier–Stokes equations are non-dimensionalized using an incompressible scaling for pressure, and the energy equation is used to obtain an expression for the velocity divergence. A pressure-correction approach is used to solve the resulting equations, such that the discrete divergence is constrained by the energy equation. As a result, the discrete equations analytically reduce to the incompressible equations at very low Mach number, i.e., the algorithm overcomes the acoustic time-scale limit without preconditioning or solution of an implicit system of equations. The algorithm discretely conserves kinetic energy in the incompressible inviscid limit, and is robust for inviscid compressible turbulence on the convective time-scale. These properties make it well-suited for DNS/LES of compressible turbulent flows. Results are shown for acoustic propagation, the incompressible Taylor problem, periodic shock tube problem, and isotropic turbulence.

Keywords: Compressible turbulence; Direct numerical simulation; Large-eddy simulation; All-Mach number; Non-dissipative; Discrete energy conservation

1. Introduction

Direct numerical simulation (DNS), and large-eddy simulation (LES) are three-dimensional, time-accurate approaches to compute turbulent fluid flows. The computational mesh and time-step in DNS

* Corresponding author. Tel.: +1 612 624 4175; fax: +1 612 626 1558.
E-mail address: mahesh@aem.umn.edu (K. Mahesh).

0021-9991/$ - see front matter © 2004 Elsevier Inc. All rights reserved.
doi:10.1016/j.jcp.2004.10.039

are fine enough that viscous dissipation is accurately computed. In contrast, LES spatially filters the Navier–Stokes equations, and directly resolves only the large-scales of motion; a subgrid model is used to account for the effect of the smaller, unresolved scales.The nonlinear nature of turbulence results in interaction between disparate length and time scales, and a broadband spectrum. As a result, numerical errors in the smallest resolved scales can affect the behavior of the entire solution. This is particularly true in LES, where the numerical method used to solve the LES equations can significantly affect the solution. Desirable requirements for a compressible algorithm for DNS/LES are therefore: (i) the ability to simulate compressible turbulence at high Reynolds numbers without loss of robustness and accuracy, (ii) the ability to efficiently and accurately compute flows with both, supersonic and highly subsonic regions, and (iii) the ability to accurately simulate flows with shock waves. This paper proposes an algorithm that addresses items (i) and (ii).

1.1. High Reynolds number

Numerical dissipation appears to be undesirable for LES (e.g. [1]), since it can suppress Reynolds number effects on the solution, and the effect of the subgrid model [2]. However, most non-dissipative schemes become unstable at high Reynolds numbers, skewed grids or flows in complex geometries. A key issue in turbulence simulation is therefore ensuring robustness without the use of numerical dissipation.

Considerable attention has been devoted to this problem for incompressible flows on structured grids. The instability has been shown to be related to aliasing errors, and influenced by the discretization of the convective term: conservative, skew-symmetric or rotational [3–5]. An attractive solution has been the development of numerical schemes that discretely conserve not only mass and momentum, but also kinetic energy in the inviscid limit [6–8]. Discrete energy conservation implies that the summation, $\sum_{cvs} u_i \partial(u_i u_j)/\partial x_j$ only has contributions from the boundary faces, and is therefore bounded. The second-order, staggered grid, Harlow–Welch algorithm [9] has this property and has been widely used for LES/DNS on structured grids. Higher-order, energy-conserving, staggered schemes for structured grids have been proposed by Morinishi et al. [10]. A colocated scheme with similar properties was developed for unstructured grids by Mahesh et al. [2] and used to perform LES in geometries ranging from flow over a cylinder to internal flow in a commercial gas-turbine combustor.

Less attention has been paid to the nonlinear stability of compressible turbulent flows. The importance of the form of the nonlinear term in the discrete equations was addressed by Blaisdell et al. [11] for Fourier spectral methods. The non-conservative form of the energy equation was found by Lee [12] to have reduced aliasing error in LES of compressible isotropic turbulence using a colocated sixth-order, finite-difference Pade scheme [13]. The colocated Pade scheme proposed by Lele has been widely and successfully used to perform DNS of compressible turbulent flows and aeroacoustics. However, the Pade scheme is prone to numerical instability in the presence of steep, unresolved gradients, or under-resolved high Reynolds turbulence. Extensions of Lele's schemes have focused on coupling them with shock-capturing schemes [14], or increased accuracy [15], and do not address the problem of nonlinear instability. Recently, Nagarajan et al. [16] have proposed a staggered variant of the original compact schemes. The staggered schemes are shown to yield stable, accurate solutions for isotropic turbulence at Reynolds numbers where the original colocated scheme is unstable. However, they note that even the staggered schemes are not stable in the absence of a subgrid model if the Reynolds number is high enough (e.g. $R_\lambda > 300$ on a 32^3 grid).

1.2. Low Mach number

The Mach number represents the ratio of acoustic to convective time-scales. Small Mach numbers therefore correspond to acoustic time-scales being much faster than convective time-scales. Numerically, this results in the compressible equations becoming very stiff as the Mach number tends to zero. Low Mach number compressible flows are common in applications involving combustion, cavitation, and even the

near-wall region of supersonic boundary layers. Preconditioning (see [17] for a review) and artificial compressibility [18,19] are possibly the most common approaches to resolve stiffness at low Mach numbers. However, preconditioned compressible equations can still prove quite expensive to solve for very small Mach number, and artificial compressibility approaches can affect time-accuracy. The short time-scale acoustics can be formally projected out using small Mach number asymptotics, which yields to lowest order, the zero Mach number equations (e.g. [20]). However, a limitation of the zero Mach number equations is the complete absence of acoustic effects; as a result they are not applicable to flows at finite Mach number.

One solution to this problem is to cast the compressible Navier–Stokes equations so that they yield the incompressible Navier–Stokes equations in the limit of small Mach number. The important differences between the incompressible and compressible equations are that for incompressible flows: (i) the absolute value of pressure is not important (ii) the velocity field is divergence-free, and (iii) the energy equation is decoupled from the continuity and momentum equations. The Mach number-dependent behavior of pressure can be treated by expressing pressure as the sum of a background value which is related to the mean speed of sound, and a fluctuating pressure which scales with the inertia of the velocity field. Such non-dimensionalization accounts for the well-known (e.g. [21]) behavior that the deviation $p - p_0 = \mathrm{O}(M^2)$, where p, p_0 and M denote the local pressure, background pressure and Mach number, respectively. Section 2 provides more details.

1.3. Motivation for proposed approach

A robust algorithm for compressible turbulence may be derived by requiring that the discrete equations reduce to the incompressible equations at low Mach numbers, and that the discretization conserves kinetic energy in the inviscid incompressible limit. The behavior of the divergence of the velocity is described by Thompson [21]. The continuity, momentum and energy equation (expressed in terms of entropy) can be rearranged to obtain

$$\frac{\partial u_j^*}{\partial x_j^*} = \frac{c_\mathrm{r}^2}{2c^2} M_\mathrm{r}^2 u_j^* \frac{\partial u_i^* u_i^*}{\partial x_j^*} + \frac{c_\mathrm{r}^2}{c^2}\frac{l_\mathrm{r}}{c_\mathrm{r} t_\mathrm{r}}\left(\frac{M_\mathrm{r}}{2}\frac{\partial u_i^* u_i^*}{\partial t^*} - \frac{1}{\rho^*}\frac{\partial p^*}{\partial t^*}\right) - \frac{c_\mathrm{r}^2}{c^2}\frac{1}{\rho^*} \times \frac{M_\mathrm{r}^2}{Re_\mathrm{r}}\left[u_j^*\frac{\partial^2 u_j^*}{\partial x_k^* \partial x_k^*} + \left(\frac{\mu_B}{\mu} + \frac{1}{3}\right) u_j^* \frac{\partial}{\partial x_j^*}\frac{\partial u_k^*}{\partial x_k^*}\right] + \frac{1}{Re_\mathrm{r}}\left(\frac{\partial v^*}{\partial T^*}\right)_p \left[(\gamma - 1) M_\mathrm{r}^2 \Gamma^* + \frac{1}{Pr}\frac{\partial^2 T^*}{\partial x_j^* \partial x_j^*}\right]. \tag{1}$$

Here, u_i, ρ, p, T denote the velocities, density, pressure and temperature, respectively, μ, μ_B and κ denote the dynamic viscosity, bulk viscosity and thermal conductivity, respectively, c denotes the speed of sound, and $\Gamma = \tau_{ij}\frac{\partial u_i}{\partial x_j}$ denotes the viscous dissipation. τ_{ij} is the viscous stress in the momentum equation. The superscript '*' denotes non-dimensional variables, and

$$u_i^* = u_i/u_\mathrm{r}, \quad x_i^* = x_i/l_\mathrm{r}, \quad p^* = p/(\rho_\mathrm{r} u_\mathrm{r} c_\mathrm{r}), \quad \rho^* = \rho/\rho_\mathrm{r}, \quad T^* = T/T_\mathrm{r},$$
$$t^* = t/t_\mathrm{r}, \quad \Gamma^* = \Gamma\left(l_\mathrm{r}^2/\mu u_\mathrm{r}^2\right). \tag{2}$$

Also, M_r and Re_r denote the Mach number and Reynolds number based on the reference state, and c_p, c_v and γ denote the specific heat at constant pressure, specific volume and ratio of specific heats, respectively. Note that the reference time-scale, t_r can be chosen to be convective ($l_\mathrm{r}/u_\mathrm{r}$) or acoustic ($l_\mathrm{r}/c_\mathrm{r}$). Eq. (1) shows that if $M_\mathrm{r} = u_\mathrm{r}/c_\mathrm{r}$ is small, and the flow is tracked on the convective time-scale ($t_\mathrm{r} = l_\mathrm{r}/u_\mathrm{r}$), then all terms on the right-hand side drop out and the velocity-field is divergence free. If on the other hand, the variation of the flow on the acoustic time-scale is sought ($t_\mathrm{r} = l_\mathrm{r}/c_\mathrm{r}$), the unsteady pressure term will produce a finite divergence. This implies that a combination of the continuity, momentum and energy equations may be used to provide a constraint on the divergence of the velocity field, which will ensure that the compressible

equations yield the incompressible equations in the limit of zero Mach number. This is the approach used in this paper to derive an algorithm, which in the limit of small Mach number is discretely energy-conserving.

The problems caused by low Mach number have been examined by the following workers. Shuen et al. [22] have developed a preconditioned, dual time-stepping method for the Navier–Stokes equations with real gas properties, and non-equilibrium chemistry. The non-conservative form of the governing equations are used. The pressure is decomposed into a background pressure which is specified, and the difference between the local pressure and background pressure is computed. Bijl and Wesseling [23] and Van der Heul et al. [24] have proposed an 'all Mach number' staggered algorithm on structured grids for the Euler equations, and inviscid MHD equations, respectively. While Bijl and Wesseling solve the energy equation in non-conservative form, a fully conservative energy equation is used by Van der Heul et al. [24]. The pressure is non-dimensionalized by scaling its deviation from a reference pressure with fluid inertia, and the energy equation is used to obtain an expression for the divergence of the velocity. The spatial discretization is dissipative for the convection terms to allow application to shock waves. A different approach was followed by Wall et al. [25], who propose a non-dissipative algorithm which eliminates acoustic stiffness by using a time-centered, implicit discretization. The implicit pressure gradient term is used to develop a pressure-correction approach, which yields a Helmholtz equation for the pressure correction.

None of the above workers examine discrete energy conservation, and the problems caused by high Reynolds number turbulence on coarse grids. This paper develops a non-dissipative algorithm that addresses the problems caused by both low Mach numbers, and high Reynolds numbers. The discrete equations are scaled such that the incompressible Navier–Stokes equations are obtained at low Mach numbers. As a result, the fast acoustic modes are analytically eliminated, and low Mach numbers can be efficiently computed. The algorithm is also constrained to discretely conserve kinetic energy in the incompressible limit. This ensures its robustness at high Reynods numbers without numerical dissipation, and for compressible flows ensures high Reynolds numbers robustness on the convective time-scale. Also, the algorithm uses a colocated storage of variables to allow easy extension to unstructured grids.

The paper is organized as follows. A description of the non-dimensional governing equations, and their regular approach to the incompressible equations is provided in Section 2. Section 2.1 describes a fully implicit, discretization of the governing equations that is centered in space and time. A predictor–corrector approach is used to solve the discrete system, and is described in Section 3. The algorithm has been implemented for parallel platforms and Cartesian grids, and Section 4 discusses numerical examples that illustrate its behavior. The examples include acoustic wave propagation, the incompressible Taylor problem, a periodic shock tube, and isotropic turbulence. A brief summary in Section 5 concludes the paper.

2. Governing equations

The governing equations are the continuity, and compressible Navier–Stokes equations for an ideal gas,

$$\frac{\partial \rho^{\mathrm{d}}}{\partial t^{\mathrm{d}}} + \frac{\partial \rho^{\mathrm{d}} u_j^{\mathrm{d}}}{\partial x_j^{\mathrm{d}}} = 0, \tag{3a}$$

$$\frac{\partial \rho^{\mathrm{d}} u_i^{\mathrm{d}}}{\partial t^{\mathrm{d}}} + \frac{\partial \rho^{\mathrm{d}} u_i^{\mathrm{d}} u_j^{\mathrm{d}}}{\partial x_j^{\mathrm{d}}} = -\frac{\partial p^{\mathrm{d}}}{\partial x_i^{\mathrm{d}}} + \frac{\partial \tau_{ij}^{\mathrm{d}}}{\partial x_j^{\mathrm{d}}}, \tag{3b}$$

$$\frac{\partial \rho^{\mathrm{d}} E^{\mathrm{d}}}{\partial t^{\mathrm{d}}} + \frac{\partial (\rho^{\mathrm{d}} E^{\mathrm{d}} + p^{\mathrm{d}}) u_j^{\mathrm{d}}}{\partial x_j^{\mathrm{d}}} = \frac{\partial \tau_{ij}^{\mathrm{d}} u_i^{\mathrm{d}}}{\partial x_j^{\mathrm{d}}} + \frac{c_p^{\mathrm{d}}}{Pr} \frac{\partial^2 \mu^{\mathrm{d}} T^{\mathrm{d}}}{\partial x_j^{\mathrm{d}} \partial x_j^{\mathrm{d}}}, \tag{3c}$$

where the superscript 'd' denotes dimensional values. The variables ρ and u_i denote the density and velocity, respectively, and $E = c_v\,T + u_i u_i/2$ denotes the total energy per unit mass. $\tau_{ij} = \mu(\frac{\partial u_i}{\partial x_j} + \frac{\partial u_j}{\partial x_i} - \frac{2}{3}\frac{\partial u_k}{\partial x_k}\delta_{ij})$ is the viscous stress tensor, c_p is the specific heat at constant pressure, and Pr denotes the Prandtl number.

The above equations are non-dimensionalized using u_r, L, ρ_r, T_r as the reference velocity, length, density and temperature, respectively. The reference pressure, $p_r = \rho_r RT_r$. The following non-dimensional variables are defined:

$$\rho = \frac{\rho^d}{\rho_r}, \quad u_i = \frac{u_i^d}{u_r}, \quad t = \frac{t^d}{L/u_r}, \quad \mu = \frac{\mu^d}{\mu_r}, \quad p = \frac{p^d - p_r}{\rho_r u_r^2}, \quad T = \frac{T^d}{T_r}, \quad \text{and} \quad M_r = \frac{u_r}{a_r} = \frac{u_r}{\sqrt{\gamma R T_r}}. \tag{4}$$

Note that the pressure has been non-dimensionalized as $p = \frac{p^d - p_r}{\rho_r u_r^2}$. Such non-dimensionalization is motivated by Thompson [21] analysis, and the work of Bijl and Wesseling [23] and van der Heul et al. [24] described in Section 1. This yields the following non-dimensional equations:

$$\frac{\partial \rho}{\partial t} + \frac{\partial \rho u_j}{\partial x_j} = 0, \tag{5a}$$

$$\frac{\partial \rho u_i}{\partial t} + \frac{\partial \rho u_i u_j}{\partial x_j} = -\frac{\partial p}{\partial x_i} + \frac{1}{Re}\frac{\partial \tau_{ij}}{\partial x_j}, \tag{5b}$$

$$M_r^2\left[\frac{\partial}{\partial t}\left(p + \frac{\gamma-1}{2}\rho u_i u_i\right) + \frac{\partial}{\partial x_j}\left(\gamma p + \frac{\gamma-1}{2}\rho u_i u_i\right)u_j\right] + \frac{\partial u_j}{\partial x_j} = \frac{(\gamma-1)M_r^2}{Re}\frac{\partial \tau_{ij} u_i}{\partial x_j} + \frac{1}{RePr}\frac{\partial}{\partial x_j}\left(\frac{\mu \partial T}{\partial x_j}\right). \tag{5c}$$

The non-dimensional equation of state is:

$$\rho T = \gamma M_r^2 p + 1. \tag{6}$$

Note that as M_r tends to zero, the energy equation (5c) requires that $\frac{\partial u_j}{\partial x_j} = \frac{1}{RePr}\frac{\partial}{\partial x_j}(\frac{\mu \partial T}{\partial x_j})$. Along with the continuity equation, this shows that the velocity field is divergence free if the density and temperature are constant. On the other hand, if the Boussinesque approximation is made, an advection–diffusion equation is obtained for temperature. The equation of state similarly reduces to $\rho T = 1$. The above non-dimensional equations therefore naturally yield the incompressible equations in the limit of very small Mach number. Also, all spatial derivatives in the above equations are in divergence form, and hence conservative. The above set of governing equations are therefore very attractive in that at high Mach numbers, they would yield the proper jump in variables across shock waves, and at very small Mach numbers, variations on the fast, acoustic time-scale would be projected out at time-steps larger than the acoustic time-scale. The primary reason for the above behavior of the non-dimensional equations is the definition of the non-dimensional pressure as $p = \frac{p^d - p_r}{\rho_r u_r^2}$. Note that alternative definitions of non-dimensional pressure as $p = p^d/(\rho_r u_r^2)$ or $p = p_d/p_r$ yield

$$\frac{\partial \rho u_i}{\partial t} + \frac{\partial \rho u_i u_j}{\partial x_j} = -\frac{1}{M_r^2}\frac{\partial p}{\partial x_i} \tag{7}$$

for the inviscid momentum equation, which is singular when M_r tend to zero.

2.1. Discretization

Fig. 1 shows the storage of variables. The Cartesian velocities, pressure and density are colocated in space at the centroids of the control volumes. Also, density, pressure and temperature are staggered in time

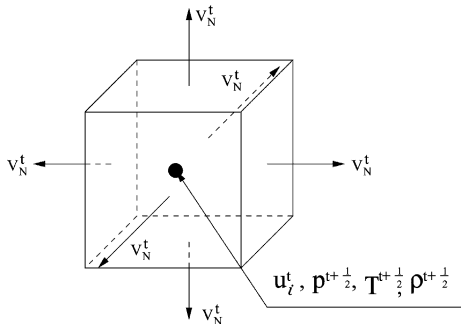

Fig. 1. Schematic of the storage of variables for a three-dimensional Cartesian control volume. The Cartesian velocities, pressure, temperature and density are stored at the centroids of the control volumes. The face-normal velocity is stored at the centers of the faces.

from velocity. This feature makes the discretization symmetric in space and time, and is essential to ensuring zero dissipation at finite time-steps. Such staggering in time was also used by Pierce and Moin [26], and Wall et al. [25] for the zero-Mach number equations, and the compressible Euler equations, respectively. The face normal velocity is located at center of the faces of the control volume and denoted by subscript v_N in this paper. As seen below, v_N is obtained by projection and not interpolation. At every time step,the velocity components u_i, and v_N are advanced from time t to $t+1$ and the thermodynamic variables, p,ρ and T are advanced from $t+\frac{1}{2}$ to $t+\frac{3}{2}$.

Integrating the governing equations over a control volume, and using Gauss' theorem to transform volume integrals into surface integrals yields the following discrete equations. The discrete continuity equation is

$$\frac{\rho_{cv}^{t+\frac{3}{2}}-\rho_{cv}^{t+\frac{1}{2}}}{\Delta t}+\frac{1}{V}\sum_{faces}\rho_{face}^{t+1}v_N^{t+1}A_{face}=0, \tag{8}$$

where ρ_{cv} denotes $\rho_{i,j,k}$, and $\sum_{faces}$ denotes summation is over all the faces of the control volume. The variables, ρ_{face} and v_N denote the density and normal velocity at each of the faces of the volume. For example $\rho_{face}=\frac{1}{2}(\rho_{i,j,k}+\rho_{i+1,j,k})$ denotes the density at the face at $i+\frac{1}{2},j,k$, and is obtained by interpolation. The corresponding face-normal velocity is $u_{i+\frac{1}{2},j,k}$ which is obtained by projection and not interpolation. The variables V and A_{face} denote the volume of the control volume and the area of the faces of the control volume. Also, ρ_{face}^{t+1} is obtained by symmetric interpolation in time, i.e., $\rho_{face}^{t+1}=(\rho_{face}^{t+\frac{1}{2}}+\rho_{face}^{t+\frac{3}{2}})/2$.

The discrete momentum equation for the i component of momentum is

$$\frac{g_{i,cv}^{t+1}-g_{i,cv}^{t}}{\Delta t}+\frac{1}{V}\sum_{faces}g_{i,face}^{t+\frac{1}{2}}v_N^{t+\frac{1}{2}}A_{face}=-\frac{\partial}{\partial x_i}p_{cv}^{t+\frac{1}{2}}+\frac{1}{Re}\frac{1}{V}\sum_{faces}\left(\tau_{ij}^{t+\frac{1}{2}}\right)_{face}N_jA_{face}. \tag{9}$$

Here, $g_i=\rho u_i$ denotes the momentum in the i direction and $(\tau_{ij})_{face}$ is the stress tensor at the face. N_j is the outward normal vector at the face. $p_{cv}^{t+\frac{1}{2}}$ is obtained by applying the trapezoidal rule to integrating the pressure-gradient term, i.e.,

$$\frac{\partial}{\partial x_i}p^{t+\frac{1}{2}}=\frac{1}{2}\left[\frac{\partial}{\partial x_i}p^{t}+\frac{\partial}{\partial x_i}p^{t+1}\right]=\frac{1}{4}\left[\frac{\partial}{\partial x_i}p^{t-\frac{1}{2}}+\frac{\partial}{\partial x_i}p^{t+\frac{1}{2}}+\frac{\partial}{\partial x_i}p^{t+\frac{1}{2}}+\frac{\partial}{\partial x_i}p^{t+\frac{3}{2}}\right]=\frac{\partial}{\partial x_i}(\overline{p}^t), \tag{10}$$

where

$$\overline{p}^t=\frac{p^{t-\frac{1}{2}}+p^{t+\frac{1}{2}}+p^{t+\frac{1}{2}}+p^{t+\frac{3}{2}}}{4}. \tag{11}$$

The gradient theorem is used to compute the pressure gradient as

$$\frac{\partial}{\partial x_i}\overline{p}^t = \frac{1}{V}\sum_{\text{faces}} \overline{p}^t_{\text{face}} N_i A_{\text{face}} = \frac{1}{V}\sum_{\text{faces}} \frac{\overline{p}^t_{\text{cv}} + \overline{p}^t_{\text{nb}}}{2} N_i A_{\text{face}} = \frac{1}{V}\sum_{\text{faces}} \frac{\overline{p}^t_{\text{nb}}}{2} N_i A_{\text{face}}. \tag{12}$$

Here, the subscript 'nb' denotes the neighboring control volume that is attached to the face under consideration. The discrete energy equation is given by

$$M_{\text{r}}^2\left[\frac{\partial}{\partial t}\left(p_{\text{cv}} + \frac{\gamma-1}{2}\rho u_i u_i\right)^{t+\frac{1}{2}} + \frac{1}{V}\sum_{\text{faces}}\left(\gamma p_{\text{cv}} + \frac{\gamma-1}{2}\rho u_i u_i\right)^{t+\frac{1}{2}}_{\text{face}} \cdot v_{\text{N}}^{t+\frac{1}{2}} A_{\text{face}}\right] + \frac{1}{V}\sum_{\text{face}} v_{\text{N}}^{t+\frac{1}{2}} A_{\text{face}}$$
$$= \frac{(\gamma-1)M_{\text{r}}^2}{Re}\frac{1}{V}\sum_{faces}\left(\tau_{ij}u_i\right)^{t+\frac{1}{2}}_{\text{face}} N_j A_{\text{face}} + \frac{1}{RePr}\frac{1}{V}\sum_{\text{faces}}\left(\mu\frac{\partial T^{t+\frac{1}{2}}}{\partial N}\right)A_{\text{face}}. \tag{13}$$

Note that the density in the momentum g has to be interpolated in time to relate the momentum and velocity, because of the time staggering between density and velocity. The central differences in time and space make the algorithm second order on regular grids. Also, the algorithm is fully implicit, and hence not limited by viscous, convective or acoustic stability limits. The discrete energy equation, shows that M_{r} and time step, Δt determine whether high frequency acoustics are captured in a time-accurate manner. At small Mach numbers, a timestep of the order of M_{r}^2 allows acoustic waves to be represented in a time-accurate manner. When high frequency acoustics are not of physical importance, the time-step may be of the order of the convective time-scale, and the energy-equation discretely projects out acoustic effects and yields zero-divergence for the velocity field.

3. Predictor–corrector method

3.1. Algorithm

A pressure-correction method is used to solve the above equations. A notable feature is that the face-normal velocities are projected to satisfy a constraint on the divergence that is determined by the energy equation. This is in contrast to most approaches that project the momentum to be constrained by the continuity equation. A result of using the energy equation to project the velocity is that at small Mach number, the projection step ensures that the velocity field is discretely divergence-free. Also as will be seen below, there is no odd–even decoupling in the incompressible limit.

An iterative approach is used to solve the continuity, momentum and energy equations. Let k denote an iteration level in an outer loop which seeks to advance the the velocities from t to $t+1$ and pressure, temperature and density from $t+\frac{1}{2}$ to $t+\frac{3}{2}$. The continuity equation (Eq. (8)) shows that if the face-normal velocity in the kth iteration $v_N^{t+1,k}$ is assumed known, the resulting system of linear equations is readily solved to obtain the corresponding density at time, $t+\frac{3}{2}$. A predictor–corrector approach is used to solve the momentum and energy equations. Let

$$p^{t+\frac{3}{2},k+1} = p^{t+\frac{3}{2},k} + \delta p. \tag{14}$$

Note that the pressure correction is based on different iteration levels and converges to zero when the outer loop has converged. The predictor step advances the momentum equation using the pressure at the current iteration level, i.e.,

$$\frac{g^*_{i,\text{cv}} - g^t_{i,\text{cv}}}{\Delta t} + \frac{1}{V}\sum_{\text{faces}}\left(g^{t+\frac{1}{2},*}_{i,\text{face}} v_N^{t+\frac{1}{2},k} A_{\text{face}}\right) = -\frac{1}{4}\frac{\partial}{\partial x_i}\left(p^{t-\frac{1}{2}} + 2p^{t+\frac{1}{2}} + p^{t+\frac{3}{2},k}\right) + \frac{1}{Re}\frac{1}{V}\sum_{\text{face}}\tau^{t+\frac{1}{2},k}_{ij,\text{face}} N_j A_{\text{face}}. \tag{15}$$

Here, the superscript '*' denotes the predicted values of $(k+1)$th iteration. $g_{i,\text{face}}^{t+\frac{1}{2},*}$ is the momentum in the i-direction at the faces and is computed as

$$g_{i,\text{face}}^{t+\frac{1}{2},*} = \frac{g_{i,\text{face}}^{t} + g_{i,\text{face}}^{*}}{2}. \tag{16}$$

The corrector step is the difference between the predictor equation (15) and the exact equation (9), i.e.,

$$g_{i,\text{cv}}^{t+1,k+1} = g_{i,\text{cv}}^{*} - \frac{\Delta t}{4}\left(\frac{\partial \delta p}{\partial x_i}\right)_{\text{cv}}, \tag{17}$$

$$u_{i,\text{cv}}^{t+1,k+1} = u_{i,\text{cv}}^{*} - \frac{\Delta t}{4\rho_{\text{cv}}^{t+1}}\left(\frac{\partial \delta p}{\partial x_i}\right)_{\text{cv}}. \tag{18}$$

The dot product of Eq. (18) and the face-normal vector yields the corrector equation for the face-normal velocity:

$$v_N^{t+1,k+1} = v_N^{*} - \frac{\Delta t}{4\rho_{\text{face}}^{t+1}}\frac{\partial \delta p}{\partial N}, \tag{19}$$

where

$$v_N^{*} = \frac{(u_i^{*,i\text{cv}1} + u_i^{*,i\text{cv}2})}{2} N_i. \tag{20}$$

Here, $i$cv1 and $i$cv2 denote the control volumes on either side of the face, and N_i denotes the face-normal. Substituting the correction steps (18) and (19) in (13) converts the energy equation to a equation for δp . The specific kinetic energy

$$(u_i u_i)^{t+1,k+1} = \left(u_i^{*} - \frac{\Delta t}{4\rho_{\text{cv}}^{t+1}}\left(\frac{\partial \delta p}{\partial x_i}\right)\right)\left(u_i^{*} - \frac{\Delta t}{4\rho_{\text{cv}}^{t+1}}\left(\frac{\partial \delta p}{\partial x_i}\right)\right) = u_i^{*}u_i^{*} - \frac{\Delta t}{2\rho^{t+1}}u_i^{*}\frac{\partial \delta p}{\partial x_i} + \mathrm{O}(\delta p^2), \tag{21}$$

i.e., the 'implicit' kinetic energy is the sum of an 'explicit' kinetic energy, and corrections due to the pressure changes. Note that the higher order terms in δp are ignored. Defining δp as the difference between iterations means that δp converges to zero at each time-step, and hence the higher-order terms are negligible. If on the other hand, δp were defined as the difference in pressure at each time-step, ignoring the higher-order terms would result in pressure-splitting error.

The discrete energy equation yields an equation for δp as follows:

$$\begin{aligned}
&\frac{M_\text{r}^2}{\Delta t}\left\{\frac{p^{t+\frac{3}{2},k} + \delta p + p^{t+\frac{1}{2}}}{2} - \frac{p^{t+\frac{1}{2}} + p^{t-\frac{1}{2}}}{2} + \frac{\gamma-1}{2}\left[\rho^{t+1}(u_i u_i)^{t+1} - \rho^{t}(u_i u_i)^{t}\right]\right\} + M_\text{r}^2\frac{1}{V}\\
&\quad\times\sum_{\text{faces}}\left[\gamma\left(\overline{p}^{t} + \frac{\delta p}{4}\right) + \frac{\gamma-1}{2}\rho^{t+\frac{1}{2}}\frac{(u_i^{t+1}+u_i^{t})}{2}\frac{(u_i^{t+1}+u_i^{t})}{2}\right]_{\text{face}}\cdot\left[\frac{v_N^{*}+v_N^{t}}{2} - \frac{\Delta t}{8\rho_{\text{face}}^{t+\frac{1}{2}}}\frac{\partial \delta p}{\partial N}\right]A_{\text{face}}\\
&\quad+\frac{1}{V}\sum_{\text{faces}}\left[\frac{v_N^{*}+v_N^{t}}{2} - \frac{\Delta t}{8\rho_{\text{face}}^{t+\frac{1}{2}}}\frac{\partial \delta p}{\partial N}\right]A_{\text{face}}\\
&\quad=\frac{(\gamma-1)M_\text{r}^2}{Re}\frac{1}{V}\sum_{\text{faces}}(\tau_{ij}u_i)_{\text{face}}^{t+\frac{1}{2},k}N_j A_{\text{face}} + \frac{1}{PrRe}\sum_{\text{faces}}\mu_{\text{face}}\frac{\partial T^{t+\frac{1}{2},k}}{\partial N}A_{\text{face}}.
\end{aligned} \tag{22}$$

Let $u_i^{t+\frac{1}{2},*} = \frac{1}{2}(u_i^{*} + u_i^{t})$, $p^0 = \gamma\overline{p}^{t} + \frac{\gamma-1}{2}\rho^{t+\frac{1}{2}}(u_i^{t+\frac{1}{2},*}u_i^{t+\frac{1}{2},*})$ and $v_N^{t+\frac{1}{2},*} = \frac{v_N^{*}+v_N^{t}}{2}$. Substituting the kinetic energy, and arranging the resulting equation in terms of δp, yields:

$$\frac{M_r^2}{\Delta t}\left\{\frac{\delta p}{2}+\frac{p^{t+\frac{3}{2},k}-p^{t-\frac{1}{2}}}{2}+\frac{\gamma-1}{2}\left[\rho^{t+1}(u_i^* u_i^*)-\rho^t(u_i^t u_i^t)\right]-\frac{\gamma-1}{4}\Delta t\left(u_i^*\frac{\partial\delta p}{\partial x_i}\right)\right\}$$
$$+M_r^2\frac{1}{V}\sum_{\text{faces}}\left[\frac{\gamma}{4}\delta p+p^0-\frac{\gamma-1}{8}\Delta t\frac{\rho^{t+\frac{1}{2}}}{\rho^{t+1}}\left(u_i^{t+\frac{1}{2},*}\right)\frac{\partial\delta p}{\partial x_i}\right]_{\text{face}}\cdot\left(v_N^{t+\frac{1}{2},*}-\frac{\Delta t}{8\rho_{\text{face}}^{t+1}}\frac{\partial\delta p}{\partial N}\right)A_{\text{face}}$$
$$+\frac{1}{V}\sum_{\text{faces}}\left(v_N^{t+\frac{1}{2},*}-\frac{\Delta t}{8\rho_{\text{face}}^{t+\frac{1}{2}}}\frac{\partial\delta p}{\partial N}\right)A_{\text{face}}$$
$$=\frac{(\gamma-1)M_r^2}{Re}\frac{1}{V}\sum_{\text{faces}}(\tau_{ij}u_i)_{\text{face}}^{t+\frac{1}{2},k}N_jA_{\text{face}}+\frac{1}{PrRe}\sum_{\text{faces}}\mu_{\text{face}}\frac{\partial T^{t+\frac{1}{2},k}}{\partial N}A_{\text{face}}. \tag{23}$$

Expanding the product in the second term yields:

$$\left\{\frac{M_r^2}{2\Delta t}+\frac{M_r^2}{V}\sum_{\text{faces}}\left[-\frac{\gamma-1}{8}v_N^{t+\frac{1}{2},*}+\frac{\gamma}{8}v_N^{t+\frac{1}{2}}-\frac{\gamma-1}{8}\frac{\rho_{\text{face}}^{t+\frac{1}{2}}}{\rho_{\text{face}}^{t+1}}v_N^{t+\frac{1}{2},*}\frac{u_{j,face}^{t+\frac{1}{2},*}\Delta t}{\Delta_{\text{nb}}}N_j-\frac{\Delta t p_{\text{face}}^0N_j}{8\rho_{\text{face}}^{t+1}\Delta_{\text{nb}}}\right]A_{\text{face}}-\frac{1}{V}\sum_{\text{faces}}\frac{\Delta tN_j}{8\rho_{\text{face}}^{t+1}\Delta_{\text{nb}}}A_{\text{face}}\right\}\delta p$$
$$+\frac{1}{V}\sum_{\text{faces}}\left\{M_r^2\left[-\frac{\gamma-1}{8}v_N^{t+\frac{1}{2},*}+\frac{\gamma}{8}v_N^{t+\frac{1}{2},*}+\frac{\gamma-1}{8}\frac{\rho_{\text{face}}^{t+\frac{1}{2}}}{\rho_{\text{face}}^{t+1}}v_N^{t+\frac{1}{2},*}\cdot\frac{(u_{j,face}^{t+\frac{1}{2},*})N_j\Delta t}{\Delta_{\text{nb}}}+\frac{\Delta t p_{\text{face}}^0N_j}{8\rho_{\text{face}}^{t+1}\Delta_{\text{nb}}}\right]+\frac{\Delta tN_j}{8\rho_{\text{face}}^{t+1}\Delta_{\text{nb}}}\right\}A_{\text{face}}\delta p_{\text{nb}}$$
$$=\frac{(\gamma-1)M_r^2}{Re}\frac{1}{V}\sum_{\text{faces}}(\tau_{ij}u_i)_{\text{face}}^{t+\frac{1}{2},k}N_jA_{\text{face}}+\frac{1}{P_rRe}\sum_{\text{faces}}\mu_{\text{face}}\frac{\partial T^{t+\frac{1}{2},k}}{\partial N}A_{\text{face}}$$
$$-\left\{\frac{M_r^2}{\Delta t}\left[\frac{p^{t+\frac{3}{2},k}-p^{t-\frac{1}{2}}}{2}+\frac{\gamma-1}{2}\left(\rho^{t+1}u_i^*u_i^*-\rho^tu_i^tu_i^t\right)\right]+\frac{M_r^2}{V}\sum_{\text{faces}}p_{\text{face}}^0v_N^{t+\frac{1}{2},*}A_{\text{face}}+\frac{1}{V}\sum_{\text{faces}}v_N^{t+\frac{1}{2},*}A_{\text{face}}\right\}, \tag{24}$$

which can be represented as

$$a_p\delta p+\sum_{\text{nb}}a_{\text{nb}}\delta p_{\text{nb}}=\text{RHS}. \tag{25}$$

Here, N_j is the face-normal, in the outward direction, the subscript 'nb' denotes the neighboring control volume, and $\Delta_{\text{nb}}=(\vec{x_{\text{nb}}}-\vec{x_{\text{cv}}})\cdot\vec{N}$ denotes the distance between the centers of the control volumes in the face-normal direction. Note that Δ_{nb} reduces to $\Delta x,\Delta y,\Delta z$ for neighbors in the x, y and z directions, respectively. Also, $u_i^{t+\frac{1}{2}}$ and $v_N^{t+\frac{1}{2}}$ are the Cartesian velocities in the control volumes, face-normal velocities, respectively, at time level $t+\frac{1}{2}$ and are computed as $\frac{u^*+u^t}{2}$ and $\frac{v_N^*+v_N^t}{2}$, respectively in Eq. (24). Note that Eq. (25) shows that the pressure-corrections at the nearest neighbors are coupled, i.e., odd–even decoupling is absent.

3.2. Implementation

The following iterative procedure is used to solve the above discrete equations.

1. Initialize the outer loop, i.e.,
$$u_i^{t+1,0}=u_i^t,\quad \rho^{t+\frac{3}{2},0}=\rho^{t+\frac{1}{2}},\quad T^{t+\frac{3}{2},0}=T^{t+\frac{1}{2}},\quad v_N^{t+1}=v_N^t.$$
2. Advance the continuity equation (8) to get $\rho^{t+3/2,\,k+1}$ by using the face normal velocity $v_N^{t+1,k}$.
3. Advance the momentum predictor equation (15) to get a provisional value of g_i^* by using pressure and velocity at current iteration step.
4. Obtain velocities at the control volume centers using $u_i^*=g_i^*/\rho^{t+1,k+1}$ where $\rho^{t+1,k+1}=(\rho^{t+3/2,k+1}+\rho^{t+1/2})/2$. Interpolate u_i^* to obtain v_N^* at the faces (Eq. (20)).

5. Solve the pressure correction equation (22) to get δp.
6. Update the pressure, momentum and the velocities at center of the control volumes using Eqs. (14), (17), (18), and update the face normal velocity by Eq. (19), respectively. Note that this implies that the face normal velocity is obtained from a projection and not by interpolating the cell-centered velocities.
7. Check convergence for the pressure correction, density and momentum between outer loop iterations.

A parallel, algebraic multigrid approach is used to solve the equation systems arising from each of the continuity, momentum and energy equations. The structured grid interface of the *Hypre* library (Lawrence Livermore National Laboratory 2003) is used for this purpose.

4. Numerical examples

The properties of the algorithm are illustrated for the problems of acoustic wave propagation, incompressible Taylor problem, shock tube, and high Reynolds number isotropic turbulence.

4.1. Acoustic problem

The algorithm is applied to the problem of inviscid, one-dimensional acoustic wave propagation in uniform mean flow on a periodic domain. Numerical results are used to demonstrate that the algorithm is non-dissipative and second-order in space and time. The initial conditions are specified from the analytical solution which is obtained as follows. Let

$$\rho = \rho_0 + \rho', \quad u = u_0 + u', \quad p = p_0 + p', \tag{26}$$

where the subscript '0' denotes the uniform mean flow, and the primes denote fluctuations about the mean flow. Linearizing the Euler equation and transforming coordinates, to $x' = x - u_0 t$, $\tau = t$ yields the following equations for the fluctuations:

$$\frac{\partial \rho'}{\partial \tau} = -\rho_0 \frac{\partial u'}{\partial x'}, \quad \frac{\partial u'}{\partial \tau} = -\frac{1}{\rho_0}\frac{\partial p'}{\partial x'}, \quad \frac{\partial p'}{\partial \tau} = -\frac{1}{M_0^2}\frac{\partial u'}{\partial x'}. \tag{27}$$

The above equations are readily solved using Fourier representation which yields

$$p'(x,t) = A_1 \mathrm{e}^{\mathrm{i}k\left[x-(u_0-\frac{u_0}{M_0})t\right]} + A_2 \mathrm{e}^{\mathrm{i}k\left[x-(u_0+\frac{u_0}{M_0})t\right]}, \tag{28a}$$

$$u'(x,t) = -M_0 A_1 \mathrm{e}^{\mathrm{i}k\left[x-(u_0-\frac{u_0}{M_0})t\right]} - M_0 A_2 \mathrm{e}^{\mathrm{i}k\left[x-(u_0+\frac{u_0}{M_0})t\right]}, \tag{28b}$$

and

$$p' p_0 = \gamma \frac{\rho'}{\rho_0} = \frac{\gamma}{\gamma - 1}\frac{T'}{T_0}. \tag{28c}$$

A_1 and A_2 are determined by the initial conditions, i.e.,

$$A_1 + A_2 = \hat{p}(0), \quad A_1 - A_2 = -\frac{1}{M_0}\hat{u}(0). \tag{29}$$

The solution is initialized using Eqs. (28a)–(28c), and (29). The initial amplitude is 10^{-3}, the domain is of length 2π, and the solution is advanced for a non-dimensional time of 10 (3.18 acoustic periods) at a mean Mach number of 1. Fig. 2 evaluates the algorithm for its spatial and temporal order of accuracy. The spatial accuracy is evaluated at a fixed time-step of 0.01, while varying the number of grid points from 32 to 256. The temporal accuracy is evaluated at a fixed spatial resolution of 256 points, while varying the time-step

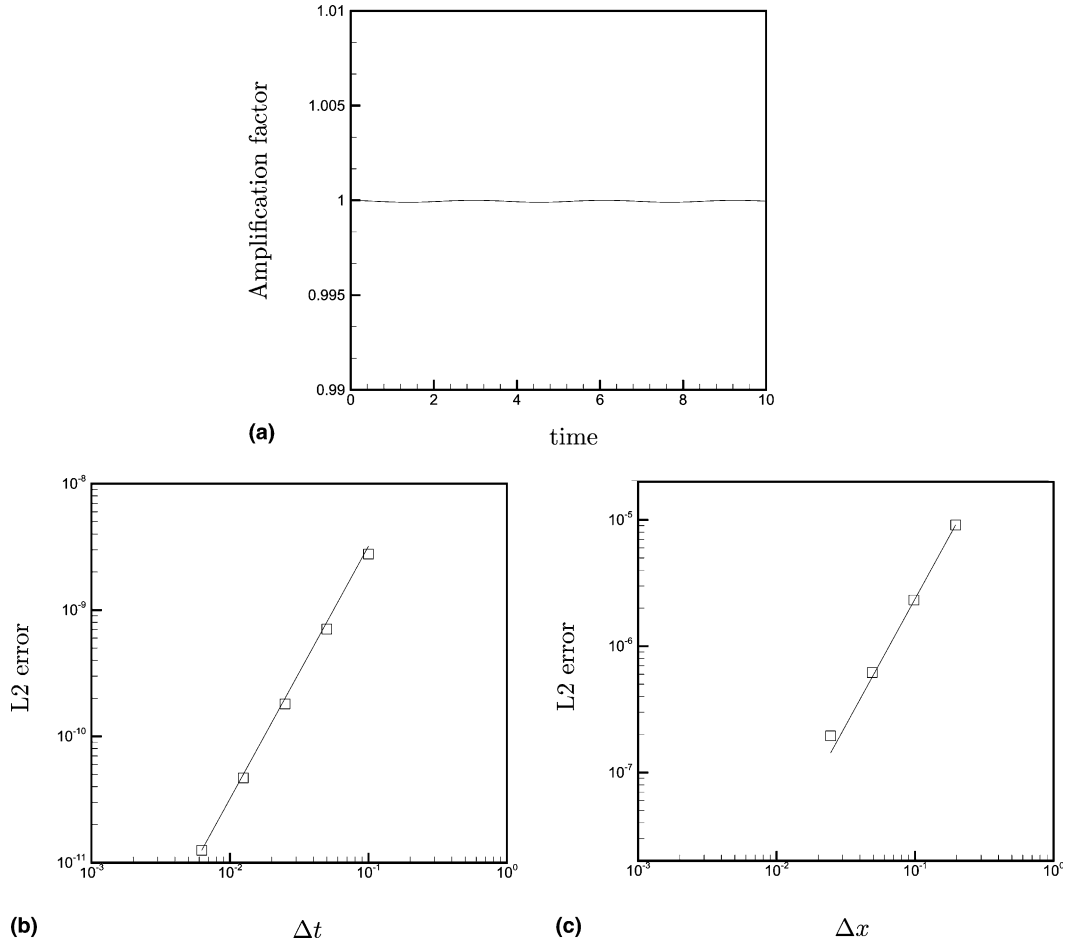

Fig. 2. Illustration of the non-dissipative nature and overall order of accuracy of the algorithm. The symbols denote the error in the computed solution, and the solid lines are straight lines with a slope of −2. (a) Amplification factor, (b) temporal order of accuracy, (c) spatial order of accuracy.

from 0.006 to 0.1. Note that second-order accuracy is obtained. An indication of computational cost is provided by the fact that for a grid with 64 points, four outer loop iterations, five continuity equation iterations, two iterations for each momentum equation, and ten iterations for the pressure-correction equation are needed to obtain a residual of 10^{-10} for the outer loop and 10^{-14} for the inner loop.

4.2. Taylor problem

Numerical solutions of the Taylor problem are used to show the ability of the algorithm to solve nearly incompressible flow without being restricted by the acoustic CFL, and to illustrate its discrete-energy conserving properties in the incompressible limit. The Taylor problem is an analytical solution to the incompressible Navier–Stokes equations which describes counter-rotating vortices that decay in time. The velocity and pressure fields are given by (for a domain of length 2π in the x- and y-directions)

$$u = -\cos x \sin y \mathrm{e}^{-2\nu t}, \quad v = \sin x \cos y \mathrm{e}^{-2\nu t}, \quad p = -\frac{1}{4}(\cos 2x + \cos 2y)\mathrm{e}^{-4\nu t}. \tag{30}$$

Fig. 3 shows numerical results for a mean Mach number of 10^{-3} obtained on a grid of $32 \times 32 \times 4$ at a time-step of 0.01 non-dimensional units. Note that this time-step corresponds to an acoustic CFl, $c_0 \Delta t/\Delta x$ of 53. The computed decay of kinetic energy is compared to analytical solution for Reynolds numbers that are varied from a value of 1 to ∞ (inviscid). Apart from agreeing with the analytical solution, note that the solution is entirely stable in the inviscid limit, and preserves its initial kinetic energy as required by the analytical solution. Central difference schemes that only conserve momentum, and not kinetic energy, would become unstable under these conditions, while schemes with numerical dissipation would decay at a rate determined by the order of the scheme, and the grid used. This behavior in the inviscid limit translates into robustness without compromising accuracy at high Reynolds numbers on grids that are too coarse to resolve viscous dissipation [2].

4.3. Shock tube problem

A periodic shock tube problem [11,27] is computed to illustrate the conservative properties of the algorithm. Fig. 4(a) shows the initial condition. The gas is initially at rest with uniform temperature, pressure and a jump in density. When the flow is advanced, the initial density discontinuity generates a shock wave (with height ρ_2, U_2, T_2 moving with speed s) and an expansion wave that moves in the opposite direction. The shock and expansion waves are separated by a contact discontinuity with height ρ_3, T_3. Fig. 4(b) shows instantaneous profiles of pressure, density and velocity at time $t = 1$ for a case where $Re = 200$. The reference Mach number $M_r = 1.0$, and the computations were performed on a domain of length 4π, using a uniform grid of 512 nodes at a time-step of 10^{-3}. The thickness of the shock wave is resolved using approximately 6 points under these conditions. The jumps in density, pressure, velocity and temperature across the shock and expansion waves are compared to analytical solution in Table 1, and seen to agree within 0.7%.

4.4. Isotropic turbulence

The algorithm is applied to simulate homogeneous, decaying isotropic turbulence on a very coarse grid without a subgrid model. This problem poses a severe test of the ability of the algorithm to ensure robustness at high Reynolds numbers without numerical dissipation. The initial fluctuation Mach number,

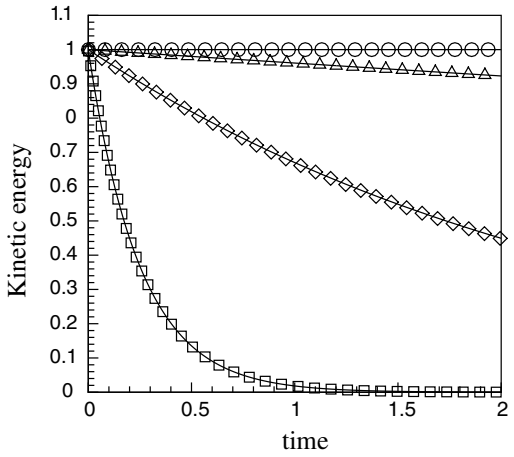

Fig. 3. Kinetic energy decay at different Reynolds numbers for the Taylor problem. The symbols denote the computed solution and are defined as follows: □, $Re = 1$; ◇, $Re = 10$; △, $Re = 100$; ○, $Re = \infty$ (inviscid). The solid lines denote the analytical solution at each Reynolds number.

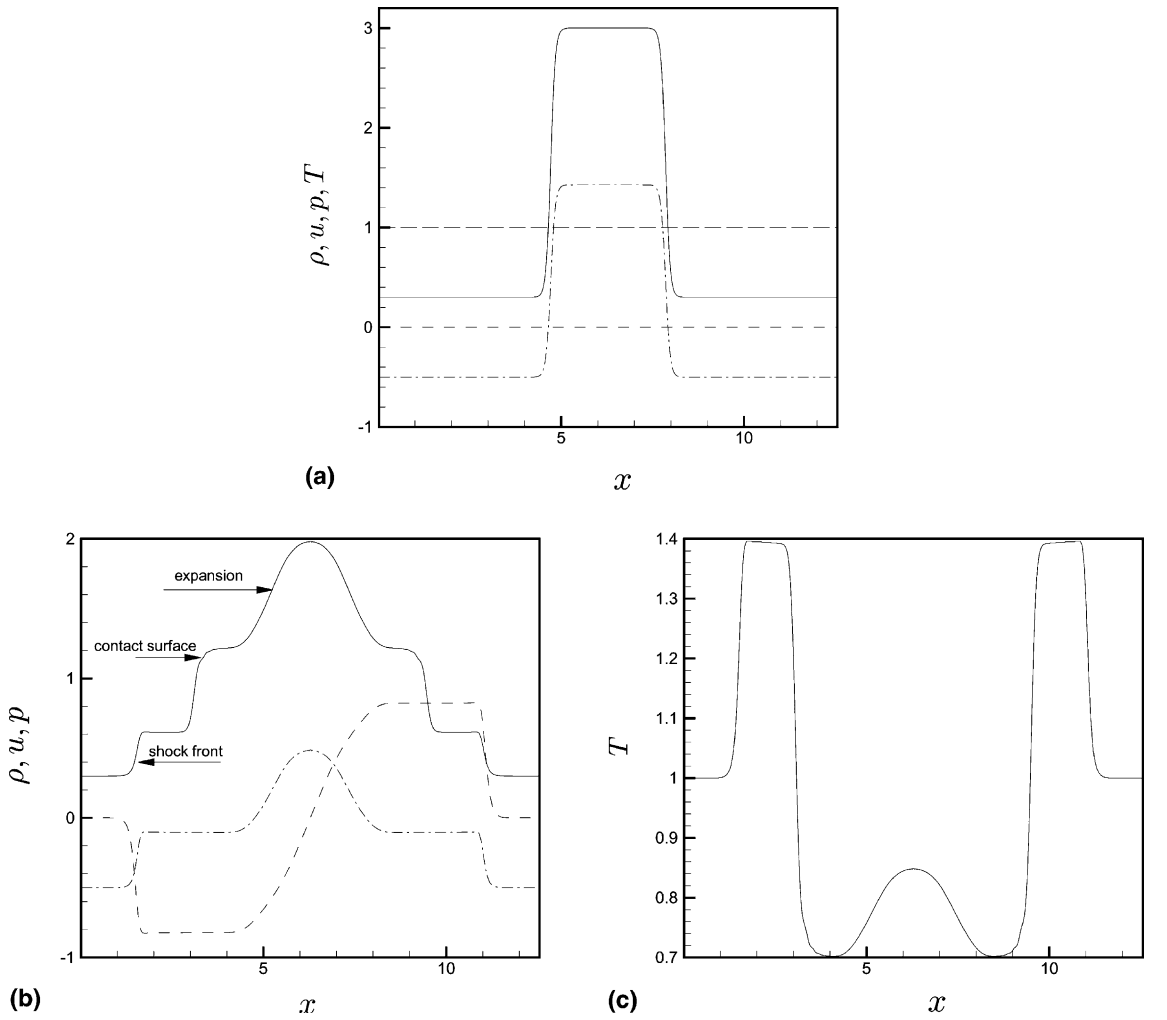

Fig. 4. (a) Initial conditions for the periodic shock tube problem: —, density; ----, velocity; –·–, pressure; ···, temperature. (b) Instantaneous solution at $t = 1.0$. —, density; ----, velocity; –·–, pressure. (c) Instantaneous temperature at $t = 1.0$.

Table 1
Comparison between predicted and calculated values for periodic shock tube

	ρ_2	ρ_3	T_2	T_3	U_2	s
Predicted	0.613	1.223	1.393	0.698	0.821	1.608
Calculated	0.614	1.214	1.394	0.702	0.821	1.590

$M_t = q/a$ and turbulent Reynolds number, $Re_\lambda = \frac{u_{rms}\lambda}{\nu}$. Here, $q = \sqrt{u_i' u_i'}$, $a = \sqrt{\gamma R T_0}$ is the mean speed of sound, and λ denotes the initial Taylor microscale. The initial radial energy spectrum is

$$E(k) = 16\sqrt{\frac{2}{\pi}}\frac{u_0^2}{k_0}\left(\frac{k}{k_0}\right)^4 e^{-2\left(\frac{k}{k_0}\right)^2}. \tag{31}$$

This initial spectrum is used to generate divergence-free, initial velocity field as suggested by Rogallo [28]. $k_0 = 5$, and the initial fluctuations in pressure, temperature and density are set to zero.

Simulations are performed for compressible ($M_t = 0.4$), and nearly incompressible ($M_t = 0.01$) conditions. For each simulation, two Reynolds numbers, ($R_\lambda = 100$ and $R_\lambda = \infty$, i.e., inviscid) are considered. The domain is $(2\pi)^3$, and the computational grid has 32 points in each direction. The time-step is fixed at 0.025τ for all the simulations. Here, τ is an 'eddy-turnover' time-scale which is equal to the initial value of λ/u_{rms}. Note that even the lower Reynolds number solution is not resolved by the computational grid. Also, no subgrid model is used.

Fig. 5 shows the decay of turbulence kinetic energy decay at different Reynolds numbers and fluctuation Mach numbers. The kinetic energy is normalized by its initial value and time is normalized by τ. Note that the solution reproduces the proper trend, i.e., reduced decay with increased Reynolds number. Also, the solution is stable in the inviscid limit. The kinetic energy decreases slightly at $M_t = 0.4$ while it is equal to its initial value for $M_t = 0.01$. This is a compressible effect; the decrease in kinetic energy at $M_t = 0.4$ is balanced by an increase in the potential energy.

An interesting aspect of homogeneous, compressible turbulence is that acoustic fluctuations generated by the initial transient will be constrained by the periodic boundary conditions, and steepen due to the nonlinearity, while decaying at a rate determined by viscosity. In the inviscid limit therefore, even the $M_t = 0.4$ and $M_t = 0.01$ flows will form shock waves in finite time. A non-dissipative, scheme will capture this behavior provided it is stable on the shock-formation time-scale. This is illustrated in Fig. 6(a) which shows the solution for very long times. Note that the $M_t = 0.4$ solution is stable for about 30τ, following which the kinetic energy, and density fluctuations increase rapidly. This behavior is due to the formation of shock waves in the domain. Fig. 6(b) shows that rms level of dilatation is comparable to that of vorticity when the kinetic energy starts increasing. In contrast the $M_t = 0.01$ flow maintains its initial kinetic energy over this considerable length of time; also the level of dilatation fluctuations is noticeably lower.

This behavior is explained by Fig. 7 which shows three-dimensional spectra of the turbulence kinetic energy for the $M_t = 0.01$ flow, and dilatation for the $M_t = 0.4$ flow. Note that the nearly incompressible flow exhibits equipartition, i.e., its spectrum at long times varies as k^2. The dilatation spectrum for the $M_t = 0.4$ flow explains its behavior at long times. Note that the levels of dilatation fluctuations increase with time, with most of the increase being at the smallest scales. This behavior is consistent with the formation of shock waves. These results therefore show that the algorithm is stable even in the inviscid limit on the

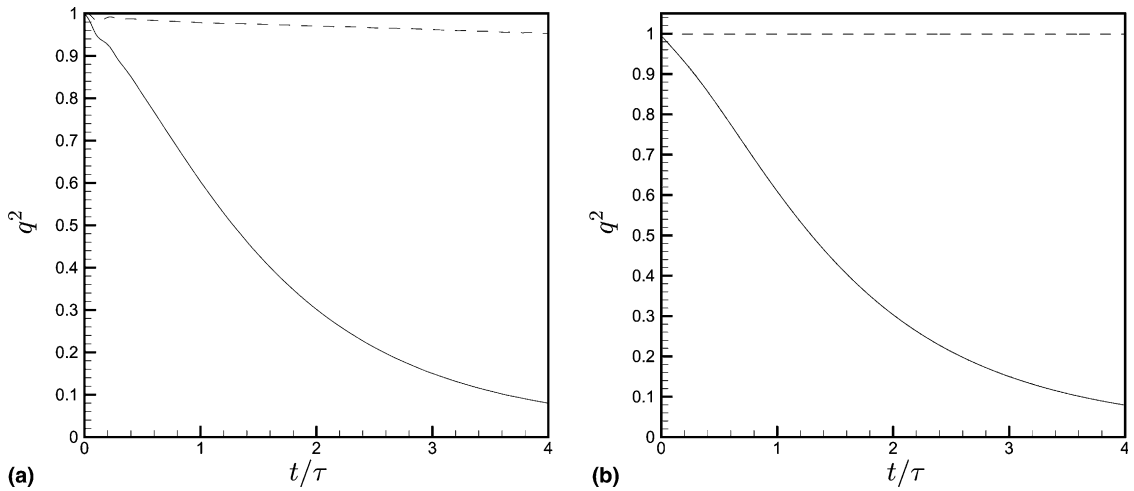

Fig. 5. Evolution of turbulence kinetic energy: (a) $M_t = 0.4$, (b) $M_t = 0.01$. For both plots — denotes $Re_\lambda = 100$, and ---- denotes inviscid flow.

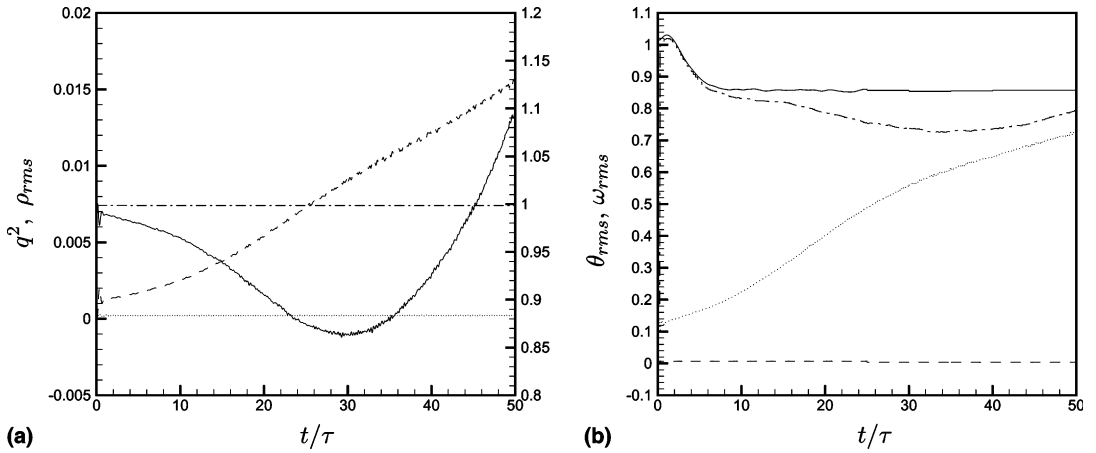

Fig. 6. Long–time evolution of inviscid, isotropic, compressible turbulence. (a) —, turbulence kinetic energy at $M_t = 0.4$; ----, rms density at $M_t = 0.4$; –·–, turbulence kinetic energy at $M_t = 0.01$; ···, rms density at $M_t = 0.01$. The range of kinetic energy is shown on the right of the plot, while the left of the plot shows the range of rms density. (b) —, rms vorticity at $M_t = 0.01$; ----, rms dilatation at $M_t = 0.01$; –·–, rms vorticity at $M_t = 0.4$; ···, rms dilatation at $M_t = 0.4$. Both quantities are normalized by the initial rms vorticity.

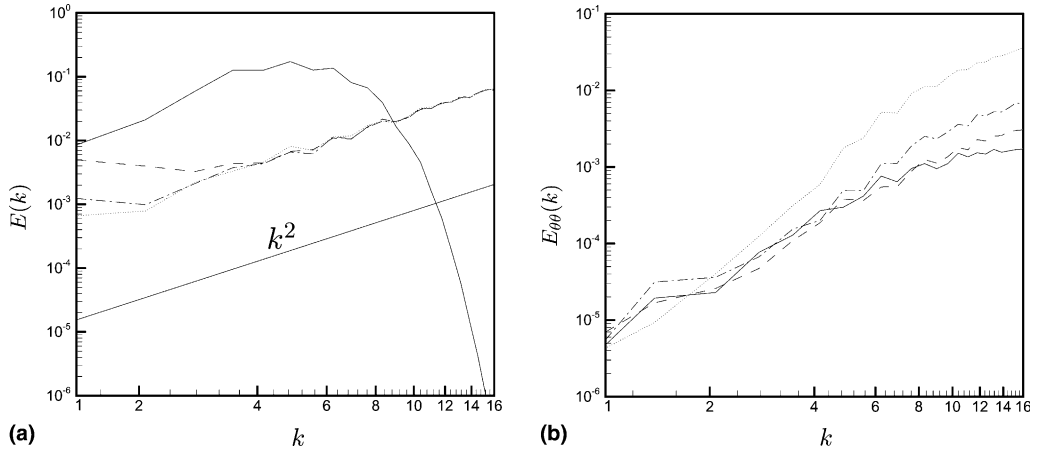

Fig. 7. Three–dimensional energy ($E(k)$) and dilatation ($E_{\theta\theta}$) spectra as a function of time for inviscid, isotropic, compressible turbulence. The energy spectrum is normalized by the initial value of q^2, and dilatation spectrum is normalized by initial ω^2_{rms}. (a) Kinetic energy spectrum for $M_t = 0.01$: —, $t/\tau = 0$; ----, $t/\tau = 5$; –·–, $t/\tau = 10$; ···, $t/\tau = 70$. (b) Dilatation spectrum for $M_t = 0.4$: —, $t/\tau = 1$; ----, $t/\tau = 4$; –·–, $t/\tau = 8$; ···, $t/\tau = 56$.

convective time-scale, and is unstable only when shock waves form. This behavior is in contrast to other commonly used non-dissipative schemes which become unstable at very short times even at very low Mach numbers, i.e., they are unstable on the convective time-scale ($t/\tau \sim 1$) at high Reynolds numbers (e.g. see Fig. 11 in [16]).

5. Conclusions

This paper proposes a non-dissipative, robust algorithm for direct numerical and large-eddy simulation of compressible turbulent flows. The algorithm colocates variables in space, to allow easy extension to

unstructured grids. The thermodynamic variables are staggered in time to ensure complete symmetry at finite time-steps. The Navier–Stokes equations are non-dimensionalized using an incompressible scaling for pressure, as a result of which the incompressible Navier–Stokes equations are recovered in the limit that the Mach number tends to zero. A pressure-correction approach is used to solve the resulting equations. The algorithm is not limited by the acoustic time-scale at low Mach numbers, and is discretely energy-conserving in the incompressible limit. Results are shown for acoustic propagation, the incompressible Taylor problem, periodic shock tube problem, and isotropic turbulence. The numerical examples suggest that the proposed approach has some very desirable features for direct numerical and large-eddy simulation of compressible turbulent flows.

Acknowledgments

This work was supported by the McKnight Land-Grant Professorship award, and the United States Department of Energy through the Stanford ASCI Alliance. Computing resources were provided by the Minnesota Supercomputing Institute and the San Diego Supercomputing Center.

References

[1] R. Mittal, P. Moin, Suitability of upwind biased schemes for large-eddy simulation, AIAA J. 30 (8) (1997) 1415–1417.
[2] K. Mahesh, G. Constantinescu, P. Moin, A numerical method for large-eddy simulation in complex geometries, J. Comput. Phys. 197 (1) (2004) 215–240.
[3] N.N. Mansour, P. Moin, W.C. Reynolds, J.H. Ferziger, Improved methods for large-eddy simulation of turbulence, in: F. Durst, B.E. Launder, F.W. Schmidt, J.H. Whitelaw (Eds.), Proceedings of the Turbulent Shear Flows I, Springer, Berlin, 1979, pp. 386–401.
[4] T.A. Zang, On the rotation and skew-symmetric forms for incompressible flow simulations, Appl. Numer. Math. 7 (1991) 27–40.
[5] A.G. Kravchenko, P. Moin, On the effect of numerical errors in large-eddy simulations of turbulent flows, J. Comput. Phys. 131 (1997) 310–322.
[6] A. Arakawa, Computational design for long term numerical integration of the equations of fluid motion: two-dimensional incompressible flow, Part I, J. Comput. Phys. 1 (1966) 119–143.
[7] J.E. Fromm, F.H. Harlow, Numerical solution of the problem of vortex street development, Phys. Fluids 6 (1963) 175–182.
[8] D.K. Lilly, On the computational stability of numerical solutions of time-dependent non-linear geophysical fluid dynamics problems, Mon. Weather Rev. 93 (1965) 11–26.
[9] F.H. Harlow, J.E. Welch, Numerical calculation of time-dependent viscous incompressible flow of fluid with free surface, Phys. Fluids 8 (1965) 2182–2189.
[10] Y. Morinishi, T.S. Lund, O.V. Vasilyev, P. Moin, Fully conservative higher order finite difference schemes for incompressible flow, J. Comput. Phys. 143 (1998) 90–124.
[11] G.A. Blaisdell, E.T. Spyropoulos, J.H. Qin, The effect of the formulation of nonlinear terms on aliasing errors in spectral methods, Appl. Numer. Math. 21 (1996) 207–219.
[12] S. Lee, Annual Research Briefs, Center for Turbulence Research, Stanford University, 1993.
[13] S.K. Lele, Compact finite-difference schemes with spectral-like resolution, J. Comput. Phys. 103 (1992) 16–42.
[14] N.A. Adams, K. Shariff, A high-resolution hybrid compact-ENO scheme for shock–turbulence interaction problems, J. Comput. Phys. 127 (1996) 27–51.
[15] K. Mahesh, A family of finite-difference schemes with good spectral resolution, J. Comput. Phys. 145 (1998) 332–358.
[16] S. Nagarajan, S.K. Lele, J.H. Ferziger, A robust high-order compact method for large eddy simulation, J. Comput. Phys. 191 (2003) 392–419.
[17] E. Turkel, Preconditioning techniques in computational fluid dynamics, Ann. Rev. Fluid Mech. 31 (1999) 385–416.
[18] A.J. Chorin, A numerical method for solving incompressible viscous flow problems, J. Comput. Phys. 2 (1967) 12–26.
[19] M. Rosenfeld, D. Kwak, Int. J. Numer. Methods Fluids 13 (10) (1991) 1311–1328.
[20] A. Majda, J.A. Sethian, The derivation and numerical solution of the equations for zero Mach number combustion, Combust. Sci. Technol. 42 (1985) 185–205.
[21] P.A. Thompson, Compressible-fluid dynamics (1988).

[22] J.S. Shuen, K.H. Chen, Y. Choi, A coupled implicit method chemical non-equilibrium flows at all speeds, J. Comput. Phys. 106 (1993) 306–318.
[23] H. Bijl, P. Wesseling, A unified method for computing incompressible and compressible flows in boundary-fitted coordinates, J. Comput. Phys. 141 (1998) 153–173.
[24] D.R. Van der Heul, C. Vuik, P. Wesseling, A conservative pressure-correction method for the Euler and ideal MHD equations at all speed, Int. J. Numer. Methods Fluids 40 (2002) 521–529.
[25] C. Wall, C.D. Pierce, P. Moin, A semi-implicit method for resolution of acoustic waves in low Mach number flows, J. Comput. Phys. 181 (2002) 545–563.
[26] C. Pierce, P. Moin, The progress variable approach for large eddy simulation of turbulent combustion, TF-Report 80, Flow Physics Division, Mechanical Engineering Department, Stanford University, Stanford, CA, 2001.
[27] T. Passot, A. Pouquet, Numerical simulation of compressible homogeneous flows in the turbulent regime, J. Fluid Mech. 181 (1987) 441–466.
[28] R. Rogallo, Numerical experiments in homogeneous turbulence, NASA Technical Memorandum TM-81315, 1981.